Evidence for Topological States and a Lifshitz Transition in Metastable $2M$-WSe_2

Yangchen He, Alex Strasser, Nicholas Hagopian, Brenna Bierman, Hongrui Ma, Carter Fox, Zizhong Li, Nicholas Pederson, Takashi Taniguchi, Kenji Watanabe, Jun Xiao, Ying Wang, Paul M. Voyles, Xiaofeng Qian, Daniel A. Rhodes**

Yangchen He, Nicholas Hagopian, Carter Fox, Zizhong Li, Nicholas Pederson, Prof. Jun Xiao, Prof. Ying Wang, Prof. Paul M. Voyles, Prof. Daniel A. Rhodes
Department of Materials Science and Engineering, University of Wisconsin-Madison, Madison, WI, 53706, US
Email Address: darhodes@wisc.edu
Alex Strasser, Prof. Xiaofeng Qian
Department of Materials Science and Engineering, Texas A&M University, College Station, TX, 77843, US
Email Address: feng@tamu.edu
Brenna Bierman
Department of Chemistry, University of Wisconsin-Madison, Madison, WI, 53706, US
Carter Fox, Prof. Jun Xiao, Prof. Ying Wang, , Prof. Daniel A. Rhodes
Department of Physics, University of Wisconsin-Madison, Madison, WI, 53706, US
Hongrui Ma, Prof. Jun Xiao, Prof. Ying Wang
Department of Electrical and Computer Engineering, University of Wisconsin-Madison, Madison, WI, 53706, US
Takashi Taniguchi, Kenji Watanabe
National Institute for Materials Science, Tsukuba, Japan

Keywords: *Topological States, Lifshitz transition, $2M$-WSe_2, Shubnikov-de Haas oscillations, Magnetotransport, 2D Semimetal.*

In recent years, T_d transition metal dichalcogenides have been heavily explored for their type-II Weyl topology, gate-tunable superconductivity, and nontrivial edge states in the monolayer limit. Here, we investigate the Fermi surface characteristics and fundamental transport properties of similarly-structured $2M$-WSe_2 bulk single crystals. Our measurements of the angular dependent Shubnikov–de Haas oscillations, with support from first-principles calculations, reveal multiple three- and two-dimensional Fermi pockets, one of which exhibits a nontrivial Berry's phase. In addition, we show that the electronic properties of $2M$-WSe_2 are similar to those of orthorhombic $MoTe_2$ and WTe_2, having a single dominant carrier type at high temperatures that evolves into coexisting electron and hole pockets with near compensation at temperatures below 100 K, suggesting the existence of a Lifshitz transition. Altogether, our observations provide evidence towards the topologically nontrivial electronic properties of $2M$-WSe_2, and motivate further investigation on the topological properties of $2M$ transition metal dichalcogenides in the atomically thin limit.

1. Introduction

A common structure type for transition metal dichalcogenides (TMDs) is the hexagonal ($2H$) structure which exhibits semiconducting behavior. $2H$-TMDs are characterized by strong spin-orbit coupling with direct band gaps between 1-2 eV in the monolayer limit [1,2]. In contrast to S- or Se-based TMDs, TMDs with heavier chalcogen elements, such as Te, typically take on orthorhombic (T_d) or monoclinic (T') structures with semimetallic behavior. T_d and T' structures exhibit a variety of interesting phenomena, including Weyl topology [3,4], quantum spin Hall insulator states [5,6,7], or superconductivity [8,9]. While the T_d and T' structures are not stable for S- and Se-based TMDs, these compounds can also be forced into a similar structure, known as "$2M$" [10,11]. The $2M$ crystal structure contains the same intralayer structure as the T' and T_d crystal structures, but the interlayer stacking order differs considerably. In T' and T_d structures, each monolayer is flipped with respect to adjacent layers. As a result, the T' and T_d unit cells can break inversion symmetry [12] in the bulk (T_d) or few-layer limit (T'). For the $2M$ structure, each neighboring monolayer is simply translated, forming a 113.2° shift between layers and taking on the centrosymmetric C2/m space group (Figure 1a).

For $1T'$-MoS_2 and $2M$-WS_2, the electronic structure exhibits a semimetallic behavior [13] with anisotropic electronic transport [14] and superconductivity at low temperatures (up to 8.8 K) [11]. With multiple band crossings at the Fermi level (E_F), $2M$-WS_2 has been suggested as a topological superconductor [11,15], while $1T'$-MoS_2 is often employed as electrical contacts to monolayer $2H$-MoS_2 [16]. Though monolayer $2M$-TMDs have been predicted to host quantum spin Hall states with sufficiently large band gaps to operate at room temperature [5,17], much is still unknown about their bulk electronic band structures. Understanding the bulk electronic band structure is an important step to determining the predicted correlated phenomena originating from the narrow overlap between electron and hole pockets at E_F and the influence of electron-electron interactions [18,19,20].

In this work, we explore the electronic band structure of $2M$-WSe_2 by measuring the temperature-dependent Shubnikov-de Haas (SdH) oscillations and carrier densities of bulk single crystals and compare these measurements to first principles calculations. We reveal a quasi-2D FS with moderately light effective mass and a nontrivial Berry's phase. Overall, our results suggest that topological states may be present near E_F and motivate further research investigating and exploiting these topological states in the few-layer limit [5].

2. Results and Discussion

Single crystals of $2M$-WSe_2 were synthesized via potassium intercalation and de-intercalation using sulfuric acid [21]. Successful synthesis of the $2M$ structure was initially confirmed by Raman and X-ray Diffraction (Supplementary Figure S1) concomitant with the metallic behavior of the temperature-dependent resistivity (Supplementary Figure S8). As synthesized crystals are commonly bundled together and are difficult to isolate without deforming by bending or twisting. In order to circumvent this issue, all bulk samples (thickness > 15 nm) characterized in this work were mechanically exfoliated via polydimethylsiloxane, and subsequently dry-transferred onto pre-patterned contacts [22]. More details can be found in the Methods section.

Similar to the $1T'$ and T_d crystal structures [12], the $2M$ crystal structure has W-chains that run along the b-axis in a zigzag pattern (perpendicular to the c-axis), while layers are stacked out-of-plane along the a-axis. For simplicity of comparing theoretical calculations to values of the experimentally measured SdH frequencies, we define a^* as the axis perpendicular to the b and c axes (Figure 1a). In order to determine the crystallographic directions of each sample, we first investigate the exfoliated flakes by measuring the intensity of the second harmonic generation (SHG) as a function of polarization angle. Although the crystal structure is centrosymmetric and, in principle, should not yield any dependence of the SHG intensity with changing polarization angle, we consistently observe an anisotropic pattern with two-fold rotational symmetry for few-layer and bulk flakes (see Figure 1b). We have also observed an enhancement of the SHG intensity with decreased sample thickness and a quadratic dependence as a function of the laser power, see Supplementary Figure S3a. These observations suggest that the observed SHG intensity is a result of broken inversion symmetry at the surface [23]. In order to correlate the angle of maximum and minimum SHG intensity to that of a particular crystallographic axis, we performed electron back scattering diffraction (EBSD) on the same crystal as shown in Figure 1a. By carefully comparing the SHG pattern with the Kikuchi pattern obtained from EBSD, we find that the maximum SHG intensity occurs along the $\langle 001 \rangle$ direction, while the minimum occurs along $\langle 010 \rangle$, parallel to the W chain and consistent with reports on WTe_2 and $MoTe_2$ [24,25]. Due to the anisotropic interatomic bonding strength, $2M$-WSe_2, like other $1T'$ structure-based TMDs, is prone to cleaving along the W chain and exfoliation typically yields flakes with a rectangular geometry (see Supplementary Figure S3). Following the orientations indicated by SHG, we prepared cross-sectional samples of exfoliated $2M$-WSe_2 using focused ion beam. Using high-angle annular dark-field scanning transmission electron microscopy (HAADF-STEM) along [010], we observe well-ordered interlayer stacking. As shown in Figure 1d, the W and Se columns fit with the $2M$ lattice with a well-defined angle of $113.2°$ between $\langle 001 \rangle$ and $\langle 100 \rangle$. Using high-angle annular dark-field scanning transmission electron microscopy (HAADF-STEM) along [010], shown in Figure 1e, we further confirm the $2M$ stacking order. Unlike $MoTe_2$, where considerable stacking disorder is observed [26], for $2M$-WSe_2 we observe uniform stacking over many unit cells. We note that for $2M$-WSe_2, on occasion we observed T_d-like stacking, which breaks inversion symmetry, as a form of local disorder. This disorder may also contribute to the angle-dependent SHG intensity observed in Figure 1b. Using the correlation between the SHG intensity, flake geometry, and diffraction (indicating the b-axis is parallel to the long edges), we determine the direction of pre-patterned devices (Figure 1f).

To determine the Fermi surface topology and topological nature of $2M$-WSe_2, we measured the temperature- and angular-dependent magnetoresistance (MR). Exfoliated flakes are measured using a four-terminal configuration with current biased parallel to the b axis (offset $< 7°$, Figure 1f) in combination with a spring rotator, where θ is the angle between applied magnetic field, B, and a^* axis (see Figure 1g). Figure 2a illustrates the change in MR, $\Delta\text{MR} = (\rho(B) - \rho(0))/\rho(0)$, as a function of magnetic field, B, oriented along the a^*, b, or c axes at 300 mK. With $B \parallel a^*$, the ΔMR exhibits a quadratic trend

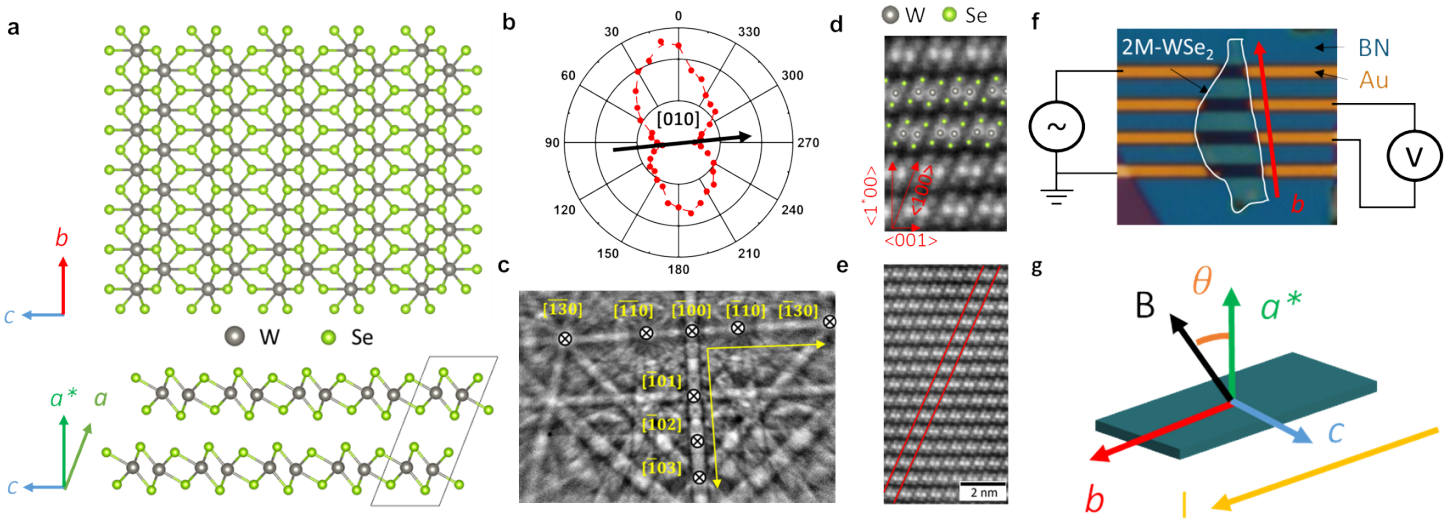

Figure 1. Crystal structure, optical characterization, and experimental setup of $2M-WSe_2$. a) Top-down view (along $a^*=c\times b$) of the in-plane crystal structure for $2M-WSe_2$ (top) and along b axis (bottom). b) Angle-dependent SHG map of a bulk $2M$-WSe_2 device. c) EBSD pattern from a $2M$-WSe_2 crystal, with Kikuchi lines indexed to the $2M$ crystal structure. d) HAADF-STEM image of $2M$-WSe_2 taken along [010] with the crystal structure overlaid. e) Zoom-out view of d) revealing the $2M$ stacking order of our WSe_2 flakes. Red lines indicate [100]. f) Optical image and g) schematic of the device and experimental setups.

up to 31 T with no sign of saturating (see Supplementary Figure S5), indicative of compensated behavior. With $B \parallel b$ or $B \parallel c$, the ΔMR exhibits a linear dependence. Both out-of-plane and in-plane trends of MR are similar to those observed in T_d-WTe_2 and T_d-$MoTe_2$ [27,28]. For the $B \parallel a^*$-dependent ΔMR, we subtracted a polynomial background and extracted the SdH signal as a function of $1/B$, as shown in the inset of Figure 2a. The SdH signal shows multiple frequencies, indicating multiple electron or hole pockets. Taking an FFT (Figure 2b) of the SdH signal for $B \parallel a^*$ reveals five frequencies: $F_\alpha = 50$ T, $F_\beta = 122$ T, $F_\gamma = 184$ T, $F_\delta = 380$ T, $F_\epsilon = 475$ T. To gain an understanding of the shape of each FS associated with these frequencies, the angle-dependent SdH signal between the a^* and b axes (as denoted by θ) at 300 mK was measured (Figure 2d). For the α pocket, the frequency remains nearly constant when tilting away from a^* and when rotating from $B \parallel c$ to $B \parallel b$ (see Supplementary Figure S7b), indicating a nearly isotropic 3D FS. To verify the isotropic morphology of the α pocket, we compare its trend to that of an ellipsoidal FS, $F(\theta)=F_1F_2/\sqrt{(F_2\cos\theta)^2+(F_1\sin\theta)^2}$, where F_1 is defined as the SdH oscillation frequency when $B \parallel a^*$, and F_2 is defined as the SdH oscillation frequency when $B \parallel b$.This ellipsoidal fitting yields a relatively small ratio of the elliptical cross-sectional areas, 1.38, for the we find that the α pocket; indicating that it is only marginally anisotropic. Similar morphology is observed for the γ and β pockets, though with increased anisotropy, suggesting that these pockets are more ellipsoidal.

Unlike the α, β, and γ pockets, for the δ and ϵ pockets, the frequency is not as constant with angle, instead taking on a $F = F_0/cos\theta$ ($B \parallel a^*$) trend that is consistent with quasi-2D FSs. For better comparison, in Figure 2d we present the fittings for ellipsoidal and quasi-2D FSs for F_δ and F_ϵ. These fittings clearly show that the δ and ϵ pockets are not 3D. We note, that ideally in order to fully describe the shape of each pocket would require SdH oscillations for all angular directions. However, we were unable to observe any oscillations from these pockets when tilting from c to b axes due to a decrease in the overall SdH amplitude [29].

To determine the topology of $2M$-WSe_2, we analyzed the amplitude for each SdH frequency as described by the Lifshitz-Kosevich (L-K) formula:

$$\Delta\rho \propto AB^{1/2}R_{\mathrm{T}}R_{\mathrm{D}}\cos(2\pi(\frac{F}{B}+\gamma-\delta))$$

where A is a constant, R_{T} is the thermal damping factor, R_{D} is the Dingle damping factor, and γ and δ are phase factors, and extract the Berry's phase (Φ_B). The value of δ depends on the dimensionality of the FS from which the SdH frequency originates. For 3D FSs, $\delta = \pm\frac{1}{8}$ for electron ($-$) and hole ($+$) pockets, and for 2D FSs, $\delta = 0$. The phase shift from γ can be defined in terms of Φ_B, with $\gamma = \frac{1}{2} - \Phi_B$. For a topologically trivial state, $\Phi_B = 0$

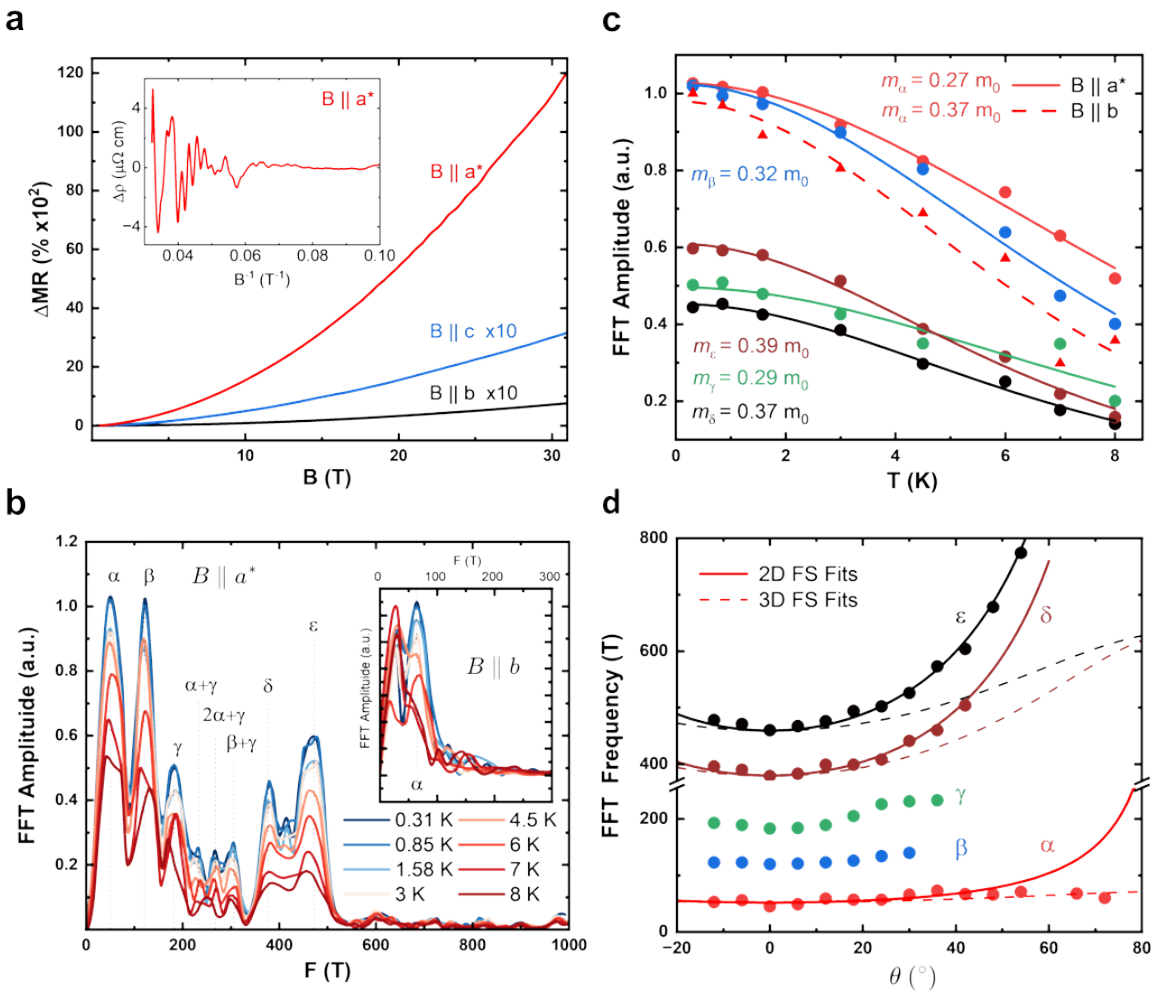

Figure 2. Temperature- and angular-dependent magnetoresistance and SdH oscillations of $2M$−WSe_2. a) ΔMR for B parallel to the a^*, b, and c axes. Inset: SdH oscillations extracted from $\rho_{xx}(B \parallel a^*)$ as a function of B^{-1} at $T = 300$ mK. b) FFT spectra obtained from SdH oscillatory component at various temperatures, with $B \parallel a^*$. Inset: Temperature-dependent FFT spectra of the SdH oscillations for $B \parallel b$. The lowest frequency(F<20 T) is attributed to the residual background. c) FFT peak amplitudes versus temperature for $B \parallel a^*$ and $B \parallel b$. Solid ($B \parallel a^*$) and dashed lines ($B \parallel b$) indicate the fits for extracting the effective masses. d) Angular dependence of the FFT peak frequencies. Fits for 2D (solid line) and ellipsoidal (dashed line) FSs are superimposed.

or 2π and for a topologically nontrivial state $\Phi_B \sim \pi$. For F_γ and F_ϵ, we find $\Phi_B = 1.24\pi$ and 0.76π, respectively, close to the nontrivial value of π. For all other frequencies, we find a trivial Berry's phase near 0 or 2π (see Supplementary Table S1).

To determine the effective mass related to each pocket, we measured the temperature dependence of the SdH oscillations. From the L-K formalism, $R_T = \lambda T/\sin(\lambda T)$, with $\lambda = 2\pi^2 k_B m^*/\hbar e B$, where m^* denotes the effective mass and $2\pi^2 k_B/\hbar e = 14.69$ TK^{-1}, we can extract the effective mass for each FS by fitting R_T for each associated SdH frequency at different temperatures. Shown in Figure 2c, we plot the normalized FFT amplitude for each SdH frequency, as a function of temperature.

For the α pocket, we find effective masses of $0.27m_0$ ($B \parallel a^*$) and $0.36m_0$ ($B \parallel b$), in agreement with the isotropic FS ascertained from the frequency angle dependence. These values are also in general agreement with the density functional theory (DFT)-calculated effective mass of $0.22m_0$ (Table S1). The effective masses for the other pockets are around the same value as the α pocket, ranging from 0.27 to $0.39m_0$.

Comparing our experimental findings to theoretical calculations, in Figure 3a we show the DFT-calculated electronic band structure for bulk $2M$-WSe_2 with spin-orbit coupling included. In agreement with the compensated behavior observed in the MR (Figure 2a), we find a semimetallic band structure with electron and hole concentrations of the same order of magnitude at E_F. Owing to the nontrivial topology of the electronic band structure, we observe band crossings very close to E_F. In Figure 3b, we map the FSs at E_F, and find two sets of closed

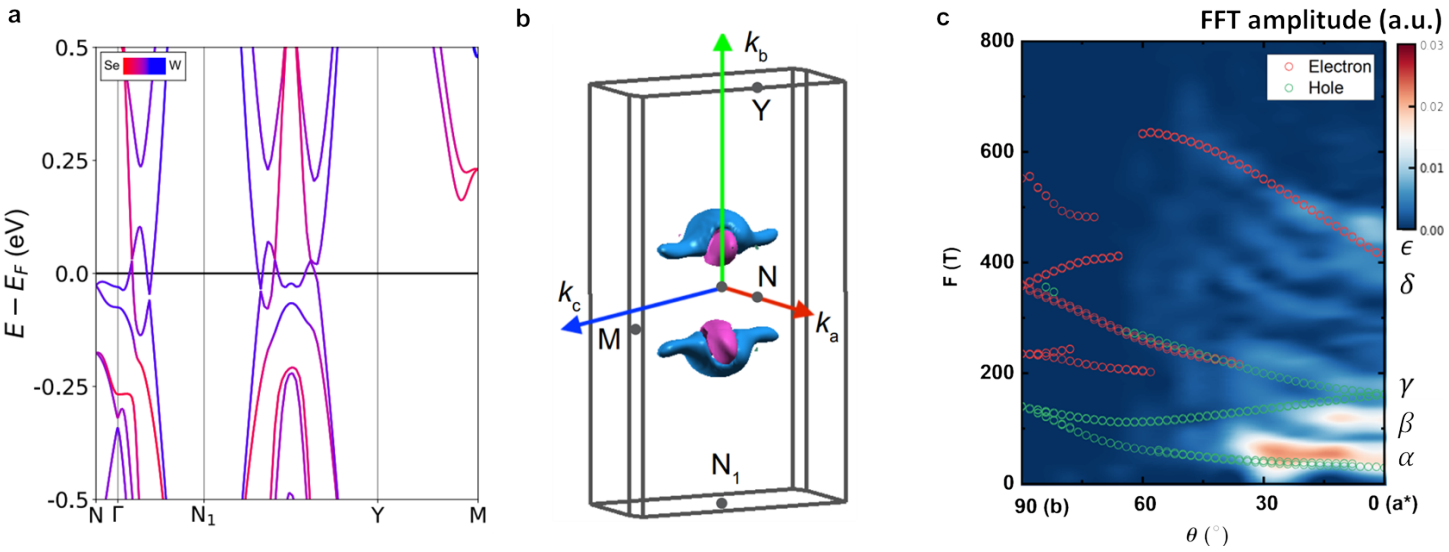

Figure 3. Electronic band structure, Fermi surface, and angular-dependent SdH oscillations of $2M-WSe_2$. a) DFT-calculated electronic band structure of $2M$-WSe_2 with the inclusion of spin-orbit coupling. b) Side view of the calculated hole (magenta) and electron (blue) FSs. c) Color map of the FFT amplitude versus frequency and magnetic field orientation with respect to the $2M$-WSe_2 crystallographic directions. Red and green circles represent the DFT-calculated SdH frequencies.

FSs, corresponding to hole (pink) and electron (blue) pockets. Both pockets are located relatively close to the Γ point and are anisotropic. However, the electron pockets are significantly more anisotropic and elongated than the hole pockets. This indicates that the oscillations with frequency F_α likely belong to the more isotropic hole pocket. Using the Onsager relation, $F_k = \phi_0 A_k/2\pi^2$, where ϕ_0 is the quantum of flux and A_k is the area of the FS cross-section perpendicular to the applied magnetic field, we calculate the angle-dependent SdH frequencies by rotating magnetic field vector, applying FS cuts that are perpendicular to the field vector, and extracting extremal orbits and corresponding SdH oscillation frequencies.

Shown in Figure 3c, we map the calculated SdH frequencies onto an interpolated map of the experimental angle-dependent SdH signal (see Supplementary Figure S7 for details). Generally, the calculated frequencies match well with the experimental frequencies, showing that the lower frequency α, β, and γ pockets are hole-like. For the higher theoretically calculated electron-like frequency, these values are close to that of the ϵ pocket. However, we instead associate this electron pocket with the δ pocket due to the anisotropic ellipsoidal shape. For our calculations, there is no value that accurately captures the 2D FS of the ϵ pocket. Overall, our analysis of the SdH oscillations suggests that the α and β pockets originate from the hole pockets and the δ peak originates from the electron pocket. The calculated FS highlighting these assignments is shown in Supplementary Figure S13. We note that there is some slight offset in the frequencies, which we expect is from a small difference in the position of the Fermi level between experiment and DFT as detailed below. Given the Berry's phase of the ϵ and γ frequencies and their lower FFT amplitudes, we expect that these frequencies are related to topologically nontrivial states. The observation of a topologically nontrivial FS is in agreement with the expectations from recent first-principles calculations and ARPES studies which propose $2M$-WSe_2 as a weak topological insulator with a bulk Dirac point near E_F [15].

In addition to the experimentally extracted nontrivial Berry phase, we perform first-principles calculations of the Z_2 topological invariants and surface states using Wannier90 [30] and WannierTools [31] to investigate the topological nature of bulk $2M$-WSe_2. The Z_2 invariants calculated by the Wannier charge center method [32] were found to be (0;110). As shown from Supplementary Figure S10, there are an odd number of Wannier charge center crossings in the k_1=0, 0.5 and k_2=0, 0.5 planes but not in the k_3=0, 0.5 planes. These theoretical results suggest that $2M$-WSe_2 is a weak topological insulator, in agreement with previous results [13,15]. We further calculated the surface states for the van der Waals surface of $2M$-WSe_2 which exhibits an overlap in the valence and conduction bands with band crossings near the Fermi level, as seen in Supplementary Figure S11. These results suggest the weak topological

insulator nature of bulk $2M$-WSe_2.

To better compare with DFT electronic structure calculations, we characterize the temperature-dependent carrier transport properties of bulk $2M$-WSe_2 via measurements of the longitudinal (ρ_{xx}) and Hall (ρ_{xy}) resistivities, as shown in Figure 4a,b. For $B = 0$ T, $2M$-WSe_2 exhibits metallic behavior down to the lowest achievable temperatures of our setup (2.5 K). At low temperatures, with magnetic field, we again observe the B^2 dependence of ρ_{xx}. This B^2 dependence gradually decreases with increasing temperature, until ∼100 K where it completely disappears. From the temperature dependence of the longitudinal resistance under varying B, we observe a saturation of the MR at a temperature T^* (see Supplementary Figure S8). With increasing B, T^* shifts to higher temperatures at a rate of 3.6 KT^{-1}, similar to the temperature-dependence of MR in T_d-$MoTe_2$ and T_d-WTe_2 [33,34]. For ρ_{xy}, we observe a nonlinear Hall signal below 50 K, suggesting major contributions from both electron and hole carriers. Going from 50 K to 100 K, we observe a significant change in ρ_{xy}, evolving into a purely linear Hall signal with hole-like behavior. Similar magnetic field- and temperature-dependent behaviors have been observed in bulk T_d-TMDs [33,34,35]. For $2M$-WSe_2, the trend of the carrier density most-closely resembles that of T_d-$NbIrTe_4$ [35] and can be attributed to a Lifshitz transition resulting from the shift of E_F toward the conduction band minima with decreasing temperature [36].

To better understand the changes in transport behavior we further analyze the transverse and longitudinal responses using the two-band semiclassical model:

$$\rho_{xx} = \frac{1}{e}\frac{(n_h\mu_h + n_e\mu_e) + (n_h\mu_e + n_e\mu_h)\mu_e\mu_h B^2}{(n_h\mu_h + n_e\mu_e)^2 + (n_h - n_e)^2\mu_e^2\mu_h^2 B^2}$$

$$\rho_{xy} = \frac{B}{e}\frac{(n_h\mu_h^2 - n_e\mu_e^2) + (n_h - n_e)\mu_e^2\mu_h^2 B^2}{(n_h\mu_h + n_e\mu_e)^2 + (n_h - n_e)^2\mu_e^2\mu_h^2 B^2}$$

where n_e and n_h are the electron and hole carrier densities, and μ_e and μ_h are the electron and hole carrier mobilities. As shown in Figure 4a,b, ρ_{xy} is well-described by the two-carrier model. By combining data gathered from fitting both ρ_{xx} and ρ_{xy} and extrapolating back from room temperature, where a single carrier dominates, we are able to get excellent fits across the entire range of temperatures. The temperature dependence of n_e, n_h, μ_e, and μ_h obtained from the fittings are shown in Figure 4c,d. At 200 K, the electron and hole mobilities are nearly the same, increasing as temperature is lowered and saturating near 15 K with $\mu_e = 1.7 \times 10^3$ $cm^2V^{-1}s^{-1}$ and $\mu_h = 5.3 \times 10^3$ $cm^2V^{-1}s^{-1}$ at 2.5 K. Using an average effective mass of $0.33m_0$ gives a mean scattering time of $\tau_t = 207$ fs. For the carrier density, at high temperature (200 K) hole carriers dominate with $n_h = 2.6 \times 10^{21}$ cm^{-3}, while the electron carrier density is four orders of magnitude smaller, consistent with the low magnetoresistance at high temperature due to a lack of carrier compensation.

As temperature decreases below 150 K, n_e increases dramatically until it nearly saturates at 50 K and reaches a density of 3.2×10^{20} cm^{-3} at 2.5 K. While for holes, the carrier density remains relatively constant, with a slight decrease to $n_h = 1.3 \times 10^{20}$ cm^{-3} at 2.5 K, giving a n_e/n_h ratio of ∼ 2.5. DFT calculations show that the energy shift of E_F required to achieve this n_e/n_h ratio is very small (15 meV), easily attainable by defects in the system. The carrier densities calculated by DFT were on the order of the experimental result, with $n_e = 1.0 \times 10^{20}$ cm^{-3} and $n_h = 4.0 \times 10^{19}$ cm^{-3}. The compensation of hole and electron carriers points to the origin of the nonsaturating magnetoresistance in $2M$-WSe_2, while the lower normalized MR at high magnetic fields (10000%) as compared to similar T' and T_d related materials likely originates from the significantly lower carrier mobilities and the imbalance between electron and hole carrier densities.

Finally, to further understand the topology of $2M$-WSe_2 and the limiting factors of the SdH amplitudes, we extract the Dingle damping factor, $R_D = e^{-\lambda T_D}$, where T_D is the Dingle temperature from fittings of the SdH oscillations, using the same L-K formalism. From T_D, we can extract a quantum scattering time, $\tau_q = h/(4\pi^2 k_B T_D)$, of 5.2 fs and a quantum mobility, $\mu_q = e\tau_q/(m^*)$, of 270 $cm^2V^{-1}s^{-1}$ (see Supplementary Table S1). These values are much smaller than the values extracted from transport measurements, yielding ratios (τ_t/τ_q, μ_t/μ_q) of ∼5 and ∼20 for electrons and holes, respectively. The differences between the values of μ and τ as extracted from the L-K formalism versus those from transport are not uncommon in topological semimetals and can be explained by a variety of mechanisms, such as electron-phonon scattering [37], chirality-protected backscattering [38], or charged impurities present in the material [39]. The large ratio of τ_t/τ_q observed in $2M$-WSe_2 likely originates from large-angle scattering due to charged impurities.

The anisotropy of the scattering can be inferred

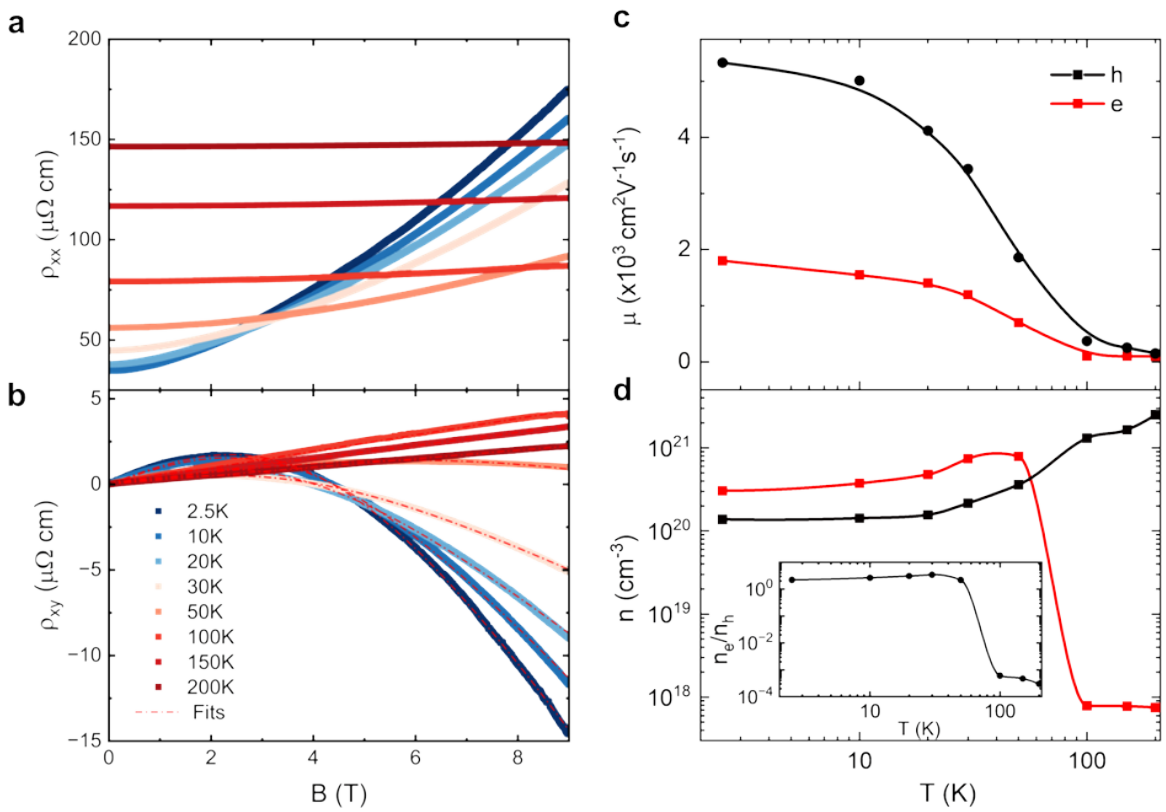

Figure 4. | Temperature-dependent carrier transport of $2M-WSe_2$. a) and b) Longitudinal (ρ_{xx}) and Hall conductivity (ρ_{xy}), respectively, as a function of B for temperature varying from 2.5 K to 200 K. Solid squares denote the experimental data and red dash lines represent fits based on the two-carrier model. c) Carrier mobility for holes (μ_h) and electrons (μ_e) as a function of T, extracted from the two-carrier-model fits from ρ_{xy}. d) Carrier densities for holes (n_h) and electrons (n_e) as a function of T obtained from two-carrier-model analysis of ρ_{xy}.

from the correlation length ξ. With a Fermi wave vector k, the ratio τ_t/τ_q depends on both k and ξ. For short range disorder $k\xi < 1$, while for long range disorder $k\xi > 1$. We can determine the in-plane effective Fermi wave vector $k_\parallel$, using the Onsager relation, $f = \frac{h}{4\pi e}k_\parallel^2$, which yields a value of $k_\parallel = 0.799$ nm^{-1}. Assuming that the value of ξ is similar to that of T_d-WTe_2 [40], we find that $k\xi \gg 1$ for $2M$-WSe_2. This indicates that the scattering in our $2M$-WSe_2 is dominated by long range disorder. Altogether, analysis of the scattering in $2M$-WSe_2 suggests that significant improvement of the crystal quality is needed in order to improve SdH amplitudes and unambiguously observe the intrinsic topological features.

3. Conclusions

By performing magnetotransport studies up to 31 T and comparing these results to first-principles calculations, we have revealed nearly compensated semimetallic behavior in bulk $2M$-WSe_2 and provided experimental evidence for the existence of a topological state near the Fermi level, similar to T_d-structured compounds. In addition, the drastic change in electron carrier density as $2M$-WSe_2 is cooled below 100 K suggests a Lifshitz transition, likely due to a shift in the chemical potential. The existence of this Lifshitz transition in $2M$-WSe_2, along with similar observations in many other materials with the same intralayer structure [34,35,36,41,42], establishes this type of transition as a general phenomenon for the semimetallic transition metal chalcogenide family, even with different stacking orders. Overall, our observations support the theoretical calculations and scanning probe measurements of few-layer $2M$-WSe_2 which propose the existence of topological states. In the few-layer limit, these topological states can be electrostatically tunable [43] and survive to high temperatures [17], creating new opportunities to realize topological devices that could survive even up to room temperature.

4. Methods Section

Synthesis: The single crystal of $2M$-WSe_2 was obtained by de-intercalation of K from the K_xWSe_2 by soaking the crystal in H_2SO_4 (0.01 M) for 48

hrs[21]. To obtain large size crystals for exfoliation, thin flakes of 2H-WSe_2 (0.1 g), grown via salt flux[44], are used as a precursor and mixed with K with a ratio of 1:0.7 in an argon-filled glove box with O_2 and H_2O <0.1 ppm. The mixture is then loaded in a Canfield crucible set before sealing in quartz under vacuum ($\sim 10^{-5}$ Torr). Subsequently, the sealed ampoule is heated to 900 °C over 1 day and held at 900 °C for 3 days, before slowly cooling down to 550 °C at a rate of 3 °C/hr. After reaching 550 °C, the furnace was turned off and the sample naturally cooled down to room temperature.

Raman Spectroscopy: Raman spectra were measured using a Horiba LabRAM HR Evolution Confocal Raman Microscope with an excitation of 633 nm and fluence of 17 mW.

Powder X-ray Diffraction (PXRD): The crystals were grounded into powder and dispensed onto a glass slide. PXRD was measured using a Bruker D8 Discovery X-ray diffractometer with a Cu-K_α source.

Second Harmonic Generation: Second harmonic generation (SHG) spectra were measured using a femtosecond pulsed laser cen-tered at 1040 nm with an 80 MHz repetition rate and $\sim$ 140 fs pulse duration (Chameleon Discovery NX, Coherent). The excitation light is linearly polarized and focused on the sample at normal incidence by a 50× long working distance objective (Mitutoyo). An average power of 1 mW was applied and the incident polarization angle was varied by rotating a half-wave plate in the incident beam path. The 520 nm SHG signal was isolated using bandpass filters and collected by a single-photon photomultiplier tube (Hamamatsu).

Electron Back-scattered Diffraction: The morphology of the samples was imaged in a Zeiss Gemini 300 FESEM. The identification of phases and crystallographic orientations was performed by EBSD using an Oxford Instruments EBSD detector and Oxford AZtec software.

Transmission Electron Microscopy: Crystallographic orientation of the sample was determined via diffraction experiments in a Technai TF30 operated at 300 keV in TEM mode. Three WSe_2 flakes were transferred onto a Au-FLAT grid with a PDMS dry transfer method. The flakes were locally viewed along their long and short rectangular edges to correlate diffraction vectors with the edge alignment. Diffraction was performed in a plan-view geometry (a^*) with respect to the flake surface, 23.2° off the crystal's a-axis. Cross-sectional samples were prepared via Ga FIB. Liftout and initial thinning were performed at 30 kV, stepping down in energy until a final thinning step at 2 kV. Immediately before characterization, the sample was plasma cleaned for 5 m at 18 W in an IBSS group MCA to minimize contamination. Samples were then transferred into a Fischione 1040 TEM Ion Mill and further thinned with Ar at 800 eV to remove extensive surface oxidation and quickly transferred into the high vacuum TEM column to minimize atmospheric oxidation. STEM characterization was performed on a ThermoFisher Titan STEM equipped with a CEOS (Corrected Electron Optical Systems) probe aberration corrector operated at 200 kV. A 23.33 mrad aperture was used for beam formation, corresponding to a beam current of roughly 22.3 pA. HAADF imaging was performed at a 160 mm camera length, corresponding to a 53.9 to 269.5 mrad collection angle range. Nonrigid registration datasets were collected by acquiring an image stack of 100, 512x512 HAADF images with a dwell time of 4 us and pixel sizes of 0.219 A. Non-rigid registration (NRR) was performed with pymatchseries software on the image stacks to minimize image artifacts arising from sample drift and scanning instabilities[45].

Device Fabrication: $2M$-WSe_2 flakes were exfoliated on to a PDMS stamp and dry-transferred onto pre-patterned electrodes (Ti/Au, 2/50 nm). Samples used for measuring SdH oscillations were placed on a 4-probe pre-pattern, while Hall samples were placed on a 6-probe pre-pattern. A top layer of hexagonal boron nitride was then transferred onto the device as a protection layer. Flake thickness was measured by atomic force microscopy yielding: 17, 29, and 31 nm for SdH oscillation samples A, B, C (see Supplementary) and 70 nm for the sample used for Hall measurements.

Magnetotransport Measurement: High-field magnetotransport measurements up to 31 T, with base temperature of 300 mK, were carried out at the National High Magnetic Field Laboratory. Hall measurements were carried out in a Quantum Design DynaCool system. All transport measurements used a lock-in preamplifier with a current of 0.5-1 μA and a frequency of 27.777-227 Hz.

First-Principles Calculations: First-principles density functional theory (DFT)[46,47] calculations were performed using Vienna Ab initio Simulation Package (VASP)[48,49], the projector augmented wave method (PAW) method[50], the Perdew-Burke-Ernzerhof (PBE) exchange-correlation energy functional[51], and a plane-wave basis with an energy cutoff of 400 eV. The crystal structure of bulk $2M$-WSe_2 was relaxed with a maximum residual force of 0.01 eV/Å, a

total energy convergence criterion of 10^{-6} eV. Relaxation and self-consistent calculations used a Monkhorst-Pack $\boldsymbol{k}$-point sampling of $3 \times 10 \times 6$ for Brillouin zone integration, while the charge carrier density calculation used a $\boldsymbol{k}$-point grid of $6 \times 20 \times 12$. To take into account the interlayer van der Waals interaction, we employed the optB88 nonlocal van der Waals density functional[52]. Spin-orbit coupling was included in all calculations except structural optimization. The electronic band structure was plotted using *pymatgen*[53]. To allow for a more accurate SdH frequency calculation, we interpolated the electronic structure from the DFT calculation in a dense grid of $60 \times 60 \times 60$ using the Wannier90 code[30] with quasiatomic orbital projection[54]. SdH frequencies and FS cuts were subsequently calculated using the Supercell K-space Extremal Area Finder (SKEAF) package[55] by rotating the B vector, applying FS cuts that are perpendicular to the field vector, and extracting extrema orbits and corresponding SdH oscillation frequencies. To investigate the topological properties of bulk $2M$-WSe_2 we calculated first-principles tight-binding Hamiltonian by using the Wannier90 code[30] and quasiatomic orbital projection[54] for bulk $2M$-WSe_2 in a primitive cell. The corresponding band structure is shown in Supplementary Figure S12. We then used this tight-binding Hamiltonian and the WannierTools package[31] to calculate the Z_2 topological invariants using the Wannier charge center method[32] and the surface states with the semi-infinite Green's function method[56].

Supporting Information

Supporting Information is available from the Wiley Online Library or from the author.

Acknowledgements

Y.H. and A.S. contributed equally to this work. We would like to acknowledge S. Benjamin and L. Balicas for valuable discussions and support. This work was primarily supported by the Department of Energy Office of Basic Energy Sciences (DE-SC0023-866), including theory (X.Q. and A.S.), measurements (D.R. and Z.L.), and analysis (Z.L., D.R., A.S., and X.Q.). C.F. and J.X. acknowledge support from the U.S. National Science Foundation (DMR-2237761). K.W. and T.T. acknowledge support from the JSPS KAKENHI (Grants No. 20H00354 and No. 23H02052) and World Premier International Research Center Initiative (WPI), MEXT, Japan. A portion of this work was performed at the National High Magnetic Field Laboratory, which is supported by National Science Foundation Cooperative Agreement No. DMR-2128556 and the State of Florida. Portions of this research were conducted with the advanced computing resources provided by Texas A&M High Performance Research Computing. Electron microscopy characterization by N.H. and P.M.V. and Polarization dependent Raman by H.M. and Y.W. were supported by the NSF through the University of Wisconsin Materials Research Science and Engineering Center (DMR-2309000). The authors gratefully acknowledge the use of facilities and instrumentation in the Wisconsin Center for Nanoscale Technology, which is partially supported by the Wisconsin Materials Research Science and Engineering Center (NSF DMR-2309000) and by the University of Wisconsin–Madison. We acknowledge the use of facilities and instrument in the Center for Nanoscale materials in Argonne National Laboratory. Work performed at the Center for Nanoscale Materials, a U.S. Department of Energy Office of Science User Facility, was supported by the U.S. DOE, Office of Basic Energy Sciences, under Contract No. DE-AC02-06CH11357. The authors are grateful to Dr. Ashley Schmidt of Bruker AXS Application Laboratory (Madison, WI) for her assistance with the X-ray data collection, processing, and interpretation.

References

[1] K. F. Mak, C. Lee, J. Hone, J. Shan, T. F. Heinz, *Phys. Rev. Lett.* **2010**, *105*, 13 136805.

[2] Q. H. Wang, K. Kalantar-Zadeh, A. Kis, J. N. Coleman, M. S. Strano, *Nat. Nanotechnol.* **2012**, *7*, 11 699.

[3] Z. Wang, D. Gresch, A. A. Soluyanov, W. Xie, S. Kushwaha, X. Dai, M. Troyer, R. J. Cava, B. A. Bernevig, *Phys. Rev. Lett.* **2016**, *117*, 5 056805.

[4] A. A. Soluyanov, D. Gresch, Z. Wang, Q. Wu, M. Troyer, X. Dai, B. A. Bernevig, *Nature* **2015**, *527*, 7579 495.

[5] X. Qian, J. Liu, L. Fu, J. Li, *Science* **2014**, *346*, 6215 1344.

[6] S. Wu, V. Fatemi, Q. D. Gibson, K. Watanabe, T. Taniguchi, R. J. Cava, P. Jarillo-Herrero, *Science* **2018**, *359*, 6371 76.

[7] Z. Fei, T. Palomaki, S. Wu, W. Zhao, X. Cai, B. Sun, P. Nguyen, J. Finney, X. Xu, D. H. Cobden, *Nat. Phys.* **2017**, *13*, 7 677.

[8] E. Sajadi, T. Palomaki, Z. Fei, W. Zhao, P. Bement, C. Olsen, S. Luescher, X. Xu, J. A. Folk, D. H. Cobden, *Science* **2018**, *362*, 6417 922.

[9] V. Fatemi, S. Wu, Y. Cao, L. Bretheau, Q. D. Gibson, K. Watanabe, T. Taniguchi, R. J. Cava, P. Jarillo-Herrero, *Science* **2018**, *362*, 6417 926.

[10] F. Wypych, K. Sollmann, R. Schöllhorn, *Mater. Res. Bull.* **1992**, *27*, 5 545.

[11] Y. Fang, J. Pan, D. Zhang, D. Wang, H. T. Hirose, T. Terashima, S. Uji, Y. Yuan, W. Li, Z. Tian, J. Xue, Y. Ma, W. Zhao, Q. Xue, G. Mu, H. Zhang, F. Huang, *Adv. Mater.* **2019**, *31*, 30 1901942.

[12] W. Dawson, D. Bullett, *J. Phys. C: Solid State Phys.* **1987**, *20*, 36 6159.

[13] Y. Fang, J. Pan, J. He, R. Luo, D. Wang, X. Che, K. Bu, W. Zhao, P. Liu, G. Mu, H. Zhang, T. Lin, F. Huang, *Angew. Chem.* **2018**, *130*, 5 1246.

[14] E. Zhang, Y.-M. Xie, Y. Fang, J. Zhang, X. Xu, Y.-C. Zou, P. Leng, X.-J. Gao, Y. Zhang, L. Ai, Y. Zhang, J. Zehao, S. Liu, J. Yan, W. Zhao, S. J. Haigh, X. Kou, J. Yang, F. Huang, K. T. Law, F. Xiu, S. Dong, *Nat. Phys.* **2023**, *19*, 1 106.

[15] L. Xu, Y. Li, Y. Fang, H. Zheng, W. Shi, C. Chen, D. Pei, D. Lu, M. Hashimoto, M. Wang, L. Yang, X. Feng, H. Zhang, F. Huang, Q. Xue, K. He, Z. Liu, Y. Chen, *Adv. Mater.* **2023**, *35*, 21 2300227.

[16] R. Kappera, D. Voiry, S. E. Yalcin, B. Branch, G. Gupta, A. D. Mohite, M. Chhowalla, *Nat. Mater.* **2014**, *13*, 12 1128.

[17] P. Chen, W. W. Pai, Y.-H. Chan, W.-L. Sun, C.-Z. Xu, D.-S. Lin, M. Chou, A.-V. Fedorov, T.-C. Chiang, *Nat. Commun.* **2018**, *9*, 1 1.

[18] D. Di Sante, P. K. Das, C. Bigi, Z. Ergönenc, N. Gürtler, J. A. Krieger, T. Schmitt, M. N. Ali, G. Rossi, R. Thomale, C. Franchini, S. Picozzi, J. Fujii, V. Strocov, G. Sangiovanni, I. Vobornik, R. Cava, G. Panaccione, *Phys. Rev. Lett.* **2017**, *119*, 2 026403.

[19] N. Xu, Z. Wang, A. Magrez, P. Bugnon, H. Berger, C. E. Matt, V. N. Strocov, N. C. Plumb, M. Radovic, E. Pomjakushina, K. Conder, J. H. Dil, R. Yu, H. Ding, M. Shi, *Phys. Rev. Lett.* **2018**, *121*, 13 136401.

[20] N. Aryal, E. Manousakis, *Phys. Rev. B: Condens. Matter* **2019**, *99*, 3 035123.

[21] X. Song, B. Hoff, R. Singha, J. W. Stiles, G. Skorupskii, J. F. Khoury, G. Cheng, F. Kamm, A. J. Uzan, S. Dulovic, S. Wu, F. Pielnhofer, N. Yao, L. M. Schoop, *Chem. Mater.* **2023**, *35*, 14 5487.

[22] R. Yang, X. Zheng, Z. Wang, C. J. Miller, P. X.-L. Feng, *J. Vac. Sci. Technol., B* **2014**, *32*, 6.

[23] F. Abtahi, P. Paul, S. Beer, A. Kuppadakkath, A. Pakhomov, A. Szeghalmi, S. Nolte, F. Setzpfandt, F. Eilenberger, *Opt. Express* **2023**, *31*, 7 11354.

[24] Q. Song, X. Pan, H. Wang, K. Zhang, Q. Tan, P. Li, Y. Wan, Y. Wang, X. Xu, M. Lin, X. Wan, F. Song, L. Dai, *Sci. Rep.* **2016**, *6*, 1 1.

[25] R. Beams, L. G. Cançado, S. Krylyuk, I. Kalish, B. Kalanyan, A. K. Singh, K. Choudhary, A. Bruma, P. M. Vora, F. Tavazza, A. V. Davydov, S. J. Stranick, *ACS Nano* **2016**, *10*, 10 9626.

[26] J. L. Hart, L. Bhatt, Y. Zhu, M.-G. Han, E. Bianco, S. Li, D. J. Hynek, J. A. Schneeloch, Y. Tao, D. Louca, P. Guo, Y. Zhu, F. Jornada, E. J. Reed, L. F. Kourkoutis, J. J. Cha, *Nat. Commun.* **2023**, *14*, 1 4803.

[27] Y. Zhao, H. Liu, J. Yan, W. An, J. Liu, X. Zhang, H. Wang, Y. Liu, H. Jiang, Q. Li, Y. Wang, X.-Z. Li, D. Mandrus, X. C. Xie, M. Pan, J. Wang, *Phys. Rev. B: Condens. Matter* **2015**, *92*, 4 041104.

[28] F. Chen, H. Lv, X. Luo, W. Lu, Q. Pei, G. Lin, Y. Han, X. Zhu, W. Song, Y. Sun, *Phys. Rev. B: Condens. Matter* **2016**, *94*, 23 235154.

[29] D. Shoenberg, *Magnetic Oscillations in Metals*, Cambridge University Press, **2009**.

[30] A. A. Mostofi, J. R. Yates, G. Pizzi, Y.-S. Lee, I. Souza, D. Vanderbilt, N. Marzari, *Computer Physics Communications* **2014**, *185*, 8 2309.

[31] Q. Wu, S. Zhang, H.-F. Song, M. Troyer, A. A. Soluyanov, *Computer Physics Communications* **2018**, *224* 405 .

[32] A. A. Soluyanov, D. Vanderbilt, *Physical Review B* **2011**, *83*, 23 235401.

[33] M. N. Ali, J. Xiong, S. Flynn, J. Tao, Q. D. Gibson, L. M. Schoop, T. Liang, N. Haldolaarachchige, M. Hirschberger, N. P. Ong, R. Cava, *Nature* **2014**, *514*, 7521 205.

[34] Q. Zhou, D. Rhodes, Q. Zhang, S. Tang, R. Schönemann, L. Balicas, *Phys. Rev. B: Condens. Matter* **2016**, *94*, 12 121101.

[35] W. Zhou, B. Li, C. Q. Xu, M. R. van Delft, Y. G. Chen, X. C. Fan, B. Qian, N. E. Hussey, X. Xu, *Adv. Electron. Mater.* **2019**, *5*, 8 1900250.

[36] J.-E. Lee, A. Wang, S. Chen, M. Kwon, J. Hwang, M. Cho, K.-H. Son, D.-S. Han, J. W. Choi, Y. D. Kim, S.-K. Mo, C. Petrovic, C. Hwang, S. Y. Park, C. Jang, H. Ryu, *Nat. Commun.* **2024**, *15*, 1 3971.

[37] G. B. Osterhoudt, Y. Wang, C. A. Garcia, V. M. Plisson, J. Gooth, C. Felser, P. Narang, K. S. Burch, *Phys. Rev. X* **2021**, *11*, 1 011017.

[38] J. Hu, S.-Y. Xu, N. Ni, Z. Mao, *Annu. Rev. Mater. Res.* **2019**, *49*, 1 207.

[39] X. Hong, K. Zou, J. Zhu, *Phys. Rev. B: Condens. Matter* **2009**, *80*, 24 241415.

[40] S. Sykora, J. Schoop, L. Graf, G. Shipunov, I. V. Morozov, S. Aswartham, B. Büchner, C. Hess, R. Giraud, J. Dufouleur, *Phys. Rev. Res.* **2020**, *2*, 3 033041.

[41] Y. Wu, N. H. Jo, M. Ochi, L. Huang, D. Mou, S. L. Bud'ko, P. Canfield, N. Trivedi, R. Arita, A. Kaminski, *Phys. Rev. Lett.* **2015**, *115*, 16 166602.

[42] Y. Jian, Q. Wu, M. Yang, Q. Feng, J. Duan, D. Chen, Q. Wang, W. Xiao, Y. Shi, O. V. Yazyev, Y. Yao, *2D Mater.* **2020**, *8*, 1 015020.

[43] L.-k. Shi, J. C. Song, *Phys. Rev. B: Condens. Matter* **2019**, *99*, 3 035403.

[44] F. A. Cevallos, S. Guo, H. Heo, G. Scuri, Y. Zhou, J. Sung, T. Taniguchi, K. Watanabe, P. Kim, H. Park, R. J. Cava, *Cryst. Growth Des.* **2019**, *19*, 10 5762.

[45] A. B. Yankovich, B. Berkels, W. Dahmen, P. Binev, S. I. Sanchez, S. A. Bradley, A. Li, I. Szlufarska, P. M. Voyles, *Nat. Commun.* **2014**, *5*, 1 4155.

[46] P. Hohenberg, W. Kohn, *Phys. Rev.* **1964**, *136* B864.

[47] W. Kohn, L. J. Sham, *Phys. Rev.* **1965**, *140* A1133.

[48] G. Kresse, J. Furthmüller, *Phys. Rev. B* **1996**, *54* 11169.

[49] G. Kresse, J. Furthmüller, *Computational Materials Science* **1996**, *6*, 1 15.

[50] P. E. Blöchl, *Physical Review B* **1994**, *50*, 24 17953.

[51] J. P. Perdew, K. Burke, M. Ernzerhof, *Physical Review Letters* **1996**, *77*, 18 3865.

[52] J. Klimeš, D. R. Bowler, A. Michaelides, *Journal of Physics: Condensed Matter* **2009**, *22*, 2 022201.

[53] S. P. Ong, W. D. Richards, A. Jain, G. Hautier, M. Kocher, S. Cholia, D. Gunter, V. L. Chevrier, K. A. Persson, G. Ceder, *Computational Materials Science* **2013**, *68* 314.

[54] X. Qian, J. Li, L. Qi, C.-Z. Wang, T.-L. Chan, Y.-X. Yao, K.-M. Ho, S. Yip, *Phys. Rev. B* **2008**, *78* 245112.

[55] S. Julian, *Comput. Phys. Commun.* **2012**, *183*, 2 324.

[56] M. L. Sancho, J. L. Sancho, J. L. Sancho, J. Rubio, *Journal of Physics F: Metal Physics* **1985**, *15*, 4 851.